Physica Scripta

PAPER

# Dielectric modulated TFET on SELBOX substrate as a label-free biosensor applications: analytical modeling study and sensitivity analysis

RECEIVED
29 July 2024

REVISED
9 September 2024

ACCEPTED FOR PUBLICATION
16 September 2024

PUBLISHED
30 September 2024

**Ashish Kumar Singh**[1], **Ramesh Kumar**[1,2] and **Satyabrata Jit**[3,*]

[1] Chitkara University Institute of Engineering and Technology, Chitkara University, Punjab, India
[2] Jadara University Research Center, Jadara University, Jordan
[3] Department of Electronics Engineering, Indian Institute of Technology, BHU, Varanasi, India
[*] Author to whom any correspondence should be addressed.

**E-mail:** sjit.ece@iitbhu.ac.in

**Keywords:** ferroelectric oxide, dielectric modulated TFET-based biosensor, SELBOX, heterojunction, BTBT, ION/IOFF sensitivity

## Abstract

The manuscript proposes a ferroelectric heterojunction TFET (BG-FE-HJ-STFET) on SELBOX substrates with a back gate to create an ultra-sensitive label-free biosensor with dielectric modulation for the detection of neutral and charged biomolecules. Within the proposed device, four cavities have been carved out for the biomolecules' immobilization under the front and rear gate dielectrics. By using a ferroelectric (FE) material as a gate stack, the low gate voltage is increased to be more effective by causing a negative capacitance phenomenon. The response of the proposed biosensor to four impartial biomolecules with different dielectric constants: protein ($k = 8$), biotin ($k = 2.63$), 3-Aminopropyl-triethoxysilane (APTES) ($k = 3.57$), and streptavidin ($k = 0.1$) has been investigated. Deoxyribonucleic acid (DNA), a charged biomolecule, is also examined for the dielectric constant of $k = 6$ concerning both charge (negative and positive) densities. The device is simulated with the commercially available SILVACO ATLAS$^{TM}$ TCAD tool. The performance analysis relies on several figures of merit (FOMs) such as DC/RF and sensitivity (including drain current, $I_{ON}/I_{OFF}$ ratio, and subthreshold swing) for both neutral and charged biomolecules. The optimized cavity structure demonstrates a notable sensitivity in drain current ($2.7 \times 10^8$) and a significant $I_{ON}/I_{OFF}$ sensitivity ($1.42 \times 10^{11}$). One of the main problems with current biosensors is the difficulty and expense of production in the nanoscale realm.

## 1. Introduction

Ever since the invention of the first oxygen biosensor by Led and Clark in 1962 [1], there has been a lot of interest among research communities in the field of medicine and nanotechnology. A biosensor is a biological device that is self-contained and used to detect biological components [1–7]. Biosensor devices have demonstrated enormous potential for their use in medical diagnostics as well as other industries such as pharmaceutical, food, drinks, environmental, agricultural, and many other biotechnological industries [1–8]. In the context of information and communication technology (ICT), ideas such as the Internet of Things (IoT) have gained a lot of interest recently because of Industry 4.0. The rapid progress in the development of intelligent devices, which are essential for improving human existence, is the main cause of this increased interest [8]. It also plays a crucial part in our daily lives by allowing us to link many sorts of smart devices via wireless technology, greatly raising our life quality [8]. In recent years, researchers all over the world have been paying close attention to FET-based biosensors because of their remarkable qualities, which include label-free detection, small size, fast response time, and reliability [9]. Because FET-based label-free biosensors can detect a wide range of biological species, they have found widespread use. Field-effect transistors have been incorporated into the FET family to facilitate biomolecule detection by depending on the detection of charges between the dielectric gate and the ionic

solution [10]. Despite having improved performance, FET biosensors still possess a few limitations that are listed [5–12]:

(i) Subthreshold swing (SS) > 60 mV/decade, or the kT/q limit, greatly extends the detection time.

(ii) Low $I_{ON}/I_{OFF}$ ratio,

(iii) When DIBL (drain-induced barrier lowering) is present,

(iv) High power consumption as a result of leakage, and

(v) Presence of short channel effects (SCEs),

(vi) Restrictions of the threshold voltage's scaling with source voltage.

To address these issues, scientists began developing TFET-based biosensors, taking advantage of the devices' remarkable characteristics, such as sharp subthreshold swing and low power consumption, which come from carrier band-to-band tunneling [8–12]. A tunnel FET-based biosensor has been extensively investigated for this purpose and has shown great promise since it can provide increased sensitivity, faster response times, and less leakage, which improves energy efficiency. Moreover, it shows promise in resolving the problems commonly linked to FET-based biosensors, as previously explored in studies [7, 9, 11–13]. TFETs are limited in terms of ON-state current and ambipolar conduction, even though they outperform CMOS [14, 15]. Several altered TFET architectures have been reported to address these issues. These techniques include hetero-dielectric TFET, multigate TFET integration of negative capacitance (NC) with ferroelectric (FE) material as the gate dielectric [16], vertical TFET [17–19], gate metal work function engineering, and the addition of low bandgap material at the source side. The ferroelectric tunnel FET (FE-TFET) concept was first introduced by Lattanzio and his research team in 2010 [20]. With the addition of a ferroelectric gate stack at high temperatures, this invention increases the $I_d$ (drain) and transconductance to supreme values at or above the Curie temperature. It was possible to obtain a sharp subthreshold swing by applying the (VDE-TrFE) approach. In addition to these, we have investigated a charge-plasma-based dielectric-modulated back-gated ferroelectric heterojunction tunnel field-effect transistor on SELBOX Substrate (BG-FE-HJ-STFET) that can be used to detect biomolecules suitable metal work-function electrodes induce $P^+$ source and N+ drain regions for this purpose. Furthermore, the gate dielectric incorporates a nanogap for the effective uptake of biomolecules. Numerous important factors, including the energy band diagram, electron tunneling rate, surface potential, drain current ($I_{DS}$), subthreshold swing (*SS*), and sensitivity, were thoroughly analyzed in this study. These analyses played a critical role in assessing the device's overall efficacy and performance. In addition, the sensing capability of BG-FE-HJ-STFET-based biosensors has been analyzed. The following section's structures are as follows:

Section 2 contains the structure of the proposed device, the fabrication feasibility, and the calibration of the models; Section 3 discusses the results and their analysis; and finally, Section 4 discusses the conclusion of the present chapter.

## 2. Device under study

Figure 1 depicts the 2D cross-sectional view of BG-FE-HJ-STFET, it contains all symbols of the dimension parameters and table 1 contains the values of the mentioned symbols. In this study, we have considered a Ge/Si-based heterojunction between source and channel, which results in better BTBT and lowers the subthreshold swing (*SS*) [21]. The function of both front and back gate material is taken at 4.2 eV. The concentrations of the doping region (p+ Ge) source and drain region ($n^+$ Si) are $1 \times 10^{20}$ $cm^{-3}$ and $5 \times 10^{18}$ $cm^{-3}$, respectively.

The dual cavities of the biosensor with a thickness ($t_c$) of 8 nm are created for the front gate, and back gate of the structure as shown in figure 1. Further, 1.5 nm $SiO_2$ and 8 nm $HfO_2$ vertically stacked gate oxide is used along the channel. The design and performance analysis of the BG-FE-HJ-STFET biosensor has been done using the commercial SILVACO ATLAS$^{TM}$ TCAD tool [22]. The non-local band-to-band tunneling (BTBT) model, Auger recombination model, field-dependent mobility model, Shockley-Read-Hall generation-recombination prototypical, and Fermi–Dirac statistics model are among the fundamental models used in this work.

Calibration for the used models was performed by comparing the proposed device's simulated drain current data with investigational work based on SOI TFET drain current at $V_{DS} = 1.0$ V, $V_{DS} = 0.5$ V, $L_G$ (gate length) = 400 nm, as shown in figure 2 [23].

The suggested BG-FE-HJ-STFET can be fabricated by following the same procedures outlined in [24]. Figure 3 shows the required process flows for creating the BG-FE-HJ-STFET. To begin the fabrication process, a clean p-type Si substrate is used. The selected substrate is next covered with the buried oxide (BOX) $SiO_2$ layer by

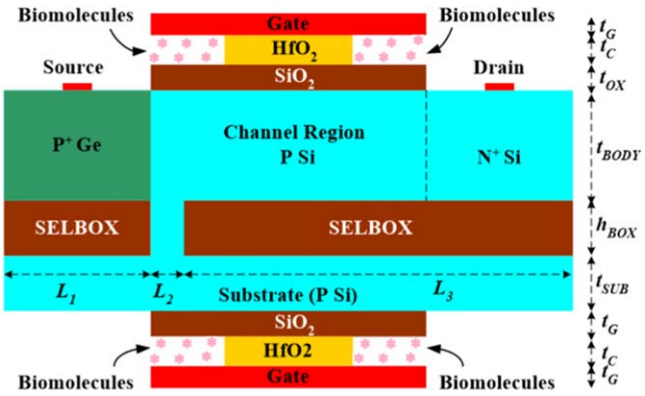


**Figure 1.** 2D schematic structures of BG-FE-HJ-STFET based biosensor.

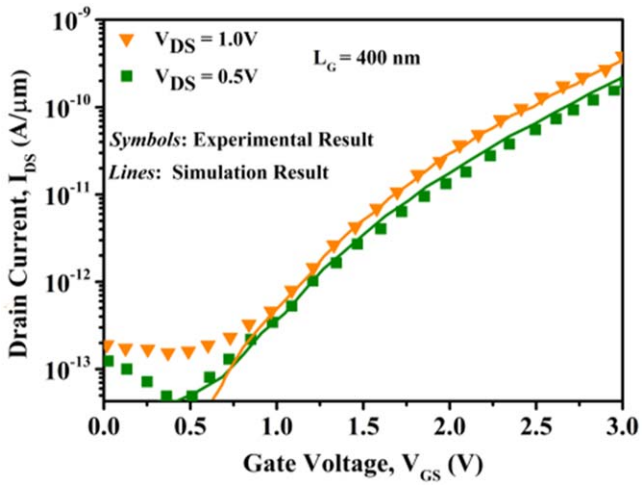


**Figure 2.** Calibration graph of the proposed structure (BG-FE-HJ-STFET) with prefabricated SOI TFET at $V_{DS} = 0.5$ V, and $V_{DS} = 1.0$ V [23].

**Table 1: Dimensional** parameters of BG-FE-HJ-STFET Biosensor.

| Symbols | Quantity | Value/units |
|---|---|---|
| *L1* | Source side BOX length | 30 nm |
| *L2* | SELBOX gap width | 2 nm |
| *L3* | Drain side BOX Length | 68 nm |
| $L_4$ | Source width | 30 nm |
| $L_5$ | Channel width | 40 nm |
| $L_6$ | Drain width | 30 nm |
| $tc = thigh\,k$ | Cavities thickness | 8 nm |
| *tox* | Low-*k* oxide thickness | 1.5 nm |
| *tG* | Gate metal thickness | 2 nm |
| *tBODY* | Channel/Body thickness | 15 nm |
| *hBOX* | Buried oxide thickness | 10 nm |
| *tSUB* | Lower substrate thickness | 10 nm |
| $k_{FE}$ | FE oxide dielectric constant | 1495 |

a thermal oxidation procedure, as shown in figures 3(a) and (b). In the third stage of the process flow, the $n^+$ Ge and $p^-$ Si layers develop over the BOX layer, and the SELBOX gap is created by etching $SiO_2$. This is accomplished by the epitaxial approach, as shown in figures 3(b) and (c). Subsequently, the channel and drain region remain intact while the silicon is etched using a masking pattern. Source and channel areas within the device are made possible by the formation of two cavities in the p-Si layer through the use of the CVD process. As

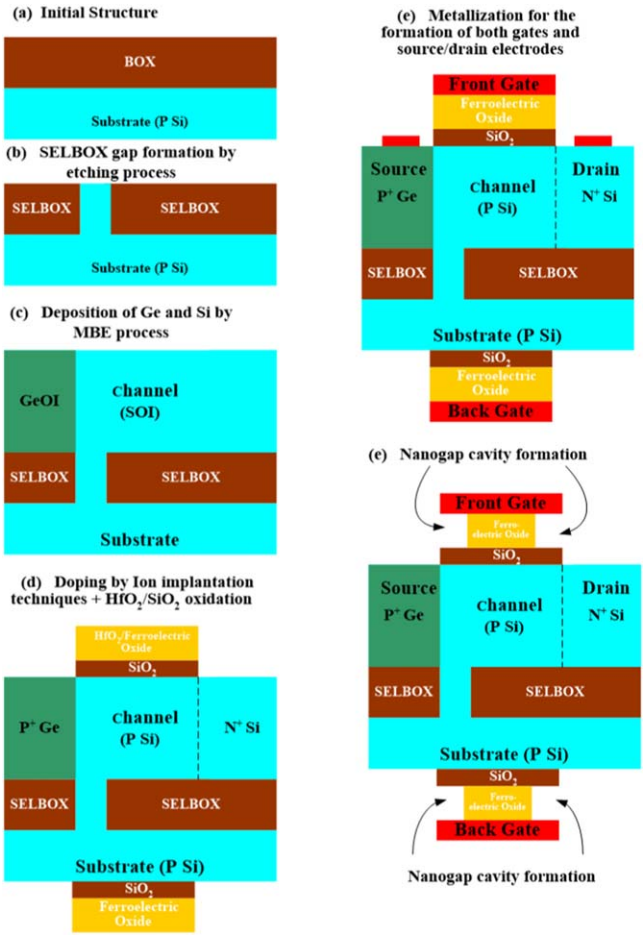


**Figure 3.** Fabrication process flows of BG-FE-HJ-STFET based biosensor.

seen in figure 3(d), this process includes the deposition of $p^+$ Ge and $n^+$ Si. After forming the source and drain regions, the appropriate doping techniques are used when the source and drain regions have been determined. The next step involves keeping the $SiO_2$/FE oxide as the gate oxide and applying metallization and design to get the gate, drain, source, and drain contacts. As shown in figure 3(d), nanocavities are then formed in the ferroelectric oxide on both sides of the gates.

## 3. Results and discussion

The results of the simulation study are shown and explained in this section. Examining biomolecules with negative, neutral, and positive charges allows one to understand how the biosensor responds to the immobilization of the biomolecules under study. To maintain the inherent advantages of a TFET, the tunneling efficiency through the bias points is increased. Therefore, at the tunnel junction, the electric field becomes much stronger when there is negative gate stack capacitance. This arrangement creates a negative capacitance (NC) effect by using a ferroelectric insulator in the gate stack in addition to the standard oxide, which acts as an intrinsic voltage amplification. As such, it increases the on-current and makes a steep sub-threshold swing (SS) easier to achieve. The subthreshold swing (*SS*) for the conventional TFET can be written as [25]:

$$SS = \ln 10\left[\frac{1}{V_{eff}}\frac{\partial V_{eff}}{\partial V_{gs}} + \frac{E+b}{E^2}\frac{\partial E}{\partial V_{gs}}\right]^{-1} \quad (1)$$

where $V_{eff}$ denotes the effective bias of a tunneling junction, $b$ is the material constant, and $E$ denotes the electric field.

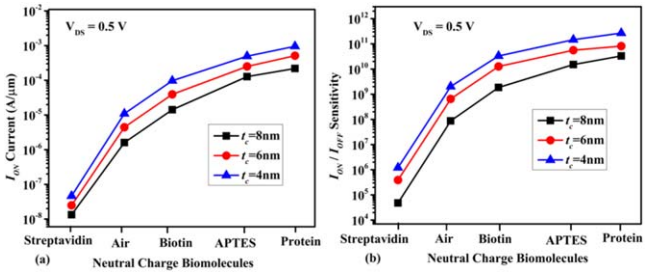


**Figure 4.** Plots of (a) on-state current, and (b) $I_{on}/I_{off}$ sensitivity of BG-FE-HJ-STFET based biosensor for studied biomolecules at $V_{DS} = 0.5$ V, $t_c = 8$ nm, $t_c = 6$ nm and $t_c = 4$ nm.

The capacitive voltage divider defines $\partial V_{gs}/\partial V_{eff}$ as follows:

$$\frac{\partial V_{gs}}{\partial V_{eff}} = 1 + \frac{C_s}{C_{ins}} \tag{2}$$

where $C_{ins}$ is the sum of the gate oxide ($C_{ins}$) and ferroelectric insulator ($C_{ferro}$) capacitances. When $V_{eff}$ exceeds $V_{gs}$, it shows the presence of the ferroelectric layer, which acts as a step-up transformer due to the development of the negative capacitance (NC) effect. Furthermore, the positive feedback effect on the capacitor's charge ($Q$) caused by the negative capacitance (NC) can be understood as an internal voltage amplification within the BG-Fe-HJ-STFET, resulting in an enhanced electric field at the tunnel junction. Consider a $V_{gs}$ (per unit area) capacitor with an applied voltage ($V_{gs}$) at the terminal and the voltage of feedback (FQ) proportional to the Q (capacitor charge).

$$Q = C_g((V_{gs} - V_{eff}) + \beta_F Q) \tag{3}$$

Where $C_{ins}$ can expressed as,

$$C_{ins} = \frac{Q}{V_{gs} - V_{eff}} = \frac{C_g}{1 - \beta_F C_g} \tag{4}$$

In accordance with equation (1), the feedback voltage must be greater than one for the negative gate-stack capacitance ($C_{ins}$) to form (i.e., ($\beta_F Q > 1$)). In other words, from equations (2) and (4), for NC to increase the internal voltage at the tunnel junction, positive feedback is required.

$$\frac{\partial V_{gs}}{\partial V_{eff}} = 1 - \frac{C_s}{C_g}(\beta_F C_g - 1) \tag{5}$$

Equation (5) indicates that the drop in $\partial V_{gs}/\partial V_{eff}$ is due to the positive feedback voltage ($\beta_F Q > 1$), which is directly related to SS as shown in equation (1). This causes SS to significantly decrease. Furthermore, as per equation (5), the presence of a positive feedback voltage facilitates the process of internal voltage amplification (( i.e. $V_{eff} > V_{gs}$). This, in turn, produces a step-up voltage transformer effect that amplifies the electric field at the tunnel junction, hence augmenting the on-current in the apparatus.

**Electrical analysis of neutral-charged biomolecules**

We describe the electrostatic properties of the suggested BG-FE-HJ-STFET biosensor in this section. In particular, we study the effects of charge density on charged biomolecules and the constant of dielectric on the behavior of neutral biomolecules. Figures 4(a) and (b) demonstrate how the proposed biosensor affects $I_{ON}$ and $I_{ON}/I_{OFF}$ sensitivity for different cavity thicknesses ($t_c$). As cavity thickness increases, the parasitic capacitance between the source and the channel decreases, resulting in a larger tunneling width at the junction. This reduces drain current and lowers $I_{ON}$ and $I_{ON}/I_{OFF}$ sensitivity, as shown in figure 4(a). The energy band diagram in figure 5(a) shows the different neutral biomolecules' on-states inside the biosensor cavity, each with a different dielectric constant. It can be shown that the sensitivity of the TFET-based biosensor increases in tandem with the biomolecule's dielectric constant, resulting in a decrease in the source/channel junction's tunneling barrier. In particular, the protein biomolecule has a somewhat lower tunneling barrier and is distinguished by a greater dielectric constant of $k = 8$. As a result, the electric field in figure 5(b) exhibits a similar pattern. The reduction in the tunneling barrier results in an increase in the electric field across the source/channel junction. Notably, as shown in figure 5(b), the protein has the largest peak of the electric field and the highest dielectric constant of all the neutral biomolecules. Figure 6(a) depicts the graphs of the surface potential of the proposed biosensor with the biomolecules at $V_{DS} = 0.5$ V. In the channel region, the surface potential is higher for a high dielectric constant. Figure 6(b) shows the plots of the transconductance of the proposed biosensor (BG-FE-HJ-STFET) for

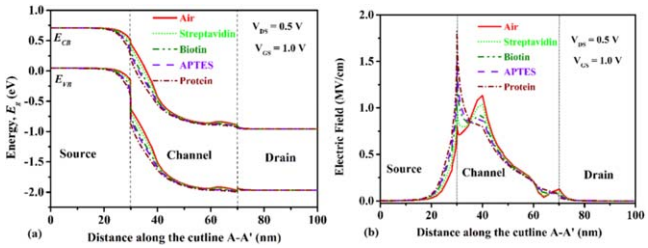


**Figure 5.** Plots of (a) on-state energy band diagram, and (b) 2D Electric field of BG-FE-HJ-STFET based biosensor at $V_{GS} = 1$ V, $V_{DS} = 0.5$ V and $t_c = 8$ nm.

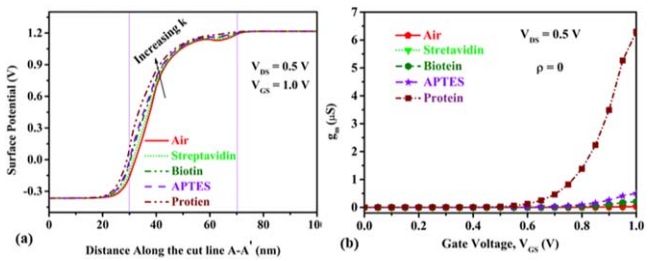


**Figure 6.** Plots of (a) surface potential and (b) transconductance of the suggested biosensor's neutral charge biomolecules for the various biomolecules at $V_{DS} = 0.5$ V.

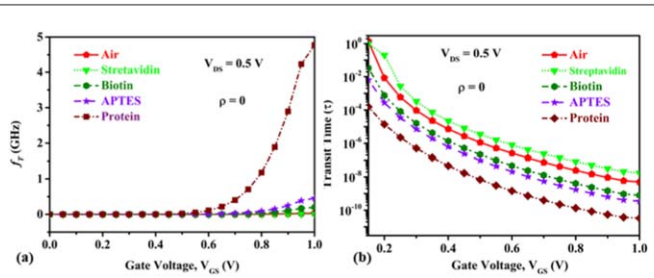


**Figure 7.** Plots of (a) cut-off frequency and (b) transit time of neutral charge biomolecules of the proposed biosensor for the different biomolecules at $V_{DS} = 0.5$ V.

the studied biomolecules. The transconductance ($g_m$) of a device describes its capacity to transfer the applied gate voltage into drain current [26]. The transconductance value for the higher dielectric constant biomolecules, such as the protein ($k = 8$), shows higher transconductance values as compared to lower dielectric constant biomolecules. Moreover, the frequency at which the current gain achieves unity in the small-signal model with a common source configuration is known as the cut-off frequency ($f_T$), and it is expressed as [26, 27]:

$$f_T = \frac{g_m}{2\pi(C_{gs} + C_{gd})} \tag{6}$$

where $g_m$ is the transconductance, $C_{gs}$ and $C_{gd}$ are the parasitic capacitances of the proposed biosensor. Figure 7(a) shows plots of cut-off frequency ($f_T$) for different biomolecules; here higher dielectric constant biomolecules show higher cut-off frequency because of higher transconductance value. Figure 7(b) shows the plots of transit time of studied neutral biomolecules at $V_{DS} = 0.5$ V.

The biosensor's transit time ($\tau$), or the amount of time it takes for charge carriers (either electrons or holes) to move between the source and drain regions, dictates the biosensor's sensing speed. The transit time ($\tau$) has the following definition [28], and it may be expressed mathematically as the reciprocal of the cut-off frequency ($f_T$):

$$\tau = \frac{1}{2\pi f_T} \tag{7}$$

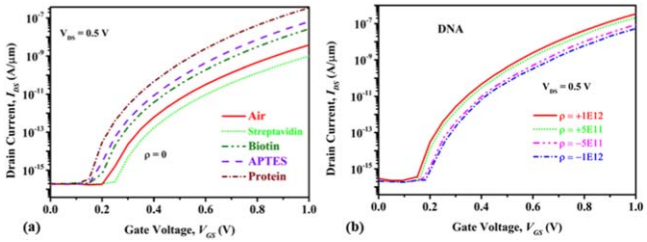


**Figure 8.** Plots showing the transfer characteristics of the BG-FE-HJ-STFET-based biosensor at $V_{DS} = 0.5$ V and $t_c = 8$ nm: (a) DNA, which is charged, and (b) biomolecules with no charge.

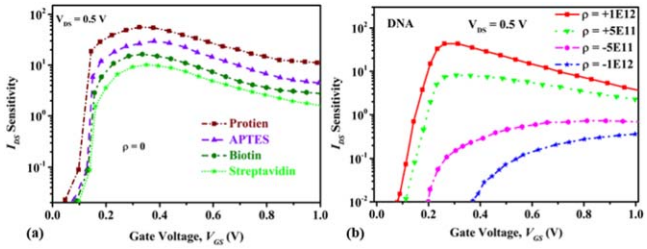


**Figure 9.** Plots of $I_{DS}$-$V_{GS}$ Sensitivity (a) neutral charge biomolecules (b) charged biomolecules (DNA) of BG-FE-HJ-STFET based biosensor at $V_{DS} = 0.5$ V and $t_c = 8$ nm.

The electron travels from the source to the drain area faster and responds better to biosensor stimulation when the dielectric constant rises from $k = 0.1$ to $k = 8$.

**Impact of (+)ve and (-)ve charged biomolecules**

Accordingly, figures 8(a) and (b) show the transfer characteristics of various charged and neutral biomolecules. Because there is a smaller tunneling barrier width and an increased electric field at the source/channel region, proteins show a greater drain current, as shown in figure 8(a). The transfer properties of DNA for various charge density levels are depicted in figure 8(b), meanwhile. In the case of DNA, there is an increase in drain current with increasing positive charge biomolecules and a decrease in drain current with increasing negative charge biomolecules [29]. The reason for this is that biomolecules with a positive charge can increase the electron population, whereas biomolecules with a negative charge can increase number of holes in the channel [30]. This section evaluates the biosensor's sensitivity by analyzing several DC parameters such as threshold voltage ($V_{th}$), subthreshold swing ($SS$), drain current ($I_{DS}$), and the $I_{ON}/I_{OFF}$ ratio. Sensitivity, which is defined in terms of electrical characteristics, is an essential criterion for the identification of target biomolecules concerning the air inside the cavity [30]. The maximum probability of detecting the targeted biomolecules is defined by higher sensitivity [29–31]. The sensitivity of the drain current is defined by equation (8) [31, 32].

$$S_{ID} = \left| \frac{(S_{ID}^{Bio} - S_{ID}^{Air})}{S_{ID}^{Air}} \right| \tag{8}$$

where the drain currents of the biosensor are denoted by the variables $I_d^{Bio}$ and $I_d^{Air}$, respectively, when the biomolecule-filled nanogap has a dielectric constant of $k > 1$ and when the nanogap is filled with air ($k = 1$).

Figure 9(a) shows the plot between drain current sensitivity and gate voltage, and figure 9(b) shows the drain current sensitivity versus gate voltage relationship, which is based on neutral and charged biomolecules. While taking various dielectric constants and charge densities (both positive and negative) into consideration. It is clear from figure 9(a) that as the dielectric constant of the biomolecules increases, so does the drain current sensitivity. When compared to all other biomolecules, streptavidin has the lowest sensitivity, while protein has the highest. The most prominent peak is seen at the lowest gate voltage, which is an essential aspect of drain current sensitivity to be aware of. The drain current sensitivity for DNA is shown in figure 9(b) for different charge density levels. Notably, the drain current sensitivity decreases with increasing concentrations of negative charge biomolecules, whereas increasing concentrations of positive charge biomolecules cause it to grow.

Equation (1) is used to compute the sensitivity of $I_{DS}$, and it is also used to calculate the sensitivity of $I_{ON}/I_{OFF}$. The $I_{ON}/I_{OFF}$ ratio rises in figure 10(a) as the dielectric constant in the nanogap cavity rises. A quicker rate of

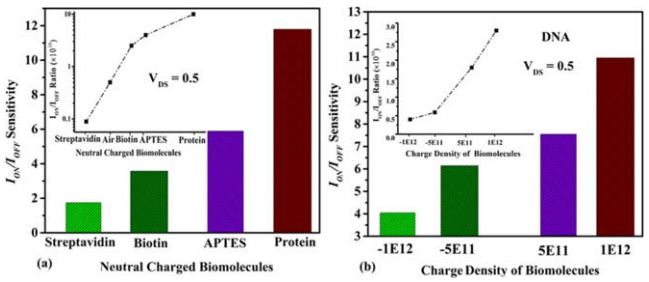


**Figure 10.** $I_{ON}/I_{OFF}$ ratio sensitivity plot of (a) neutral charge biomolecules (b) charged biomolecules (DNA).

electron tunneling from the source to the channel region results from a lowering in the tunneling barrier at the source/channel interface, which causes this rise [6]. Consequently, the protein biomolecule ($k = 8$) in the nanogap cavity has the maximum $I_{ON}/I_{OFF}$ ratio sensitivity among all neutral biomolecules. The $I_{ON}/I_{OFF}$ sensitivities of the BG-FE-HJ-STFET biosensor are depicted for five distinct values of dielectric constant ($k = 0.1$, 2.36, 3.57, 8, and 6) for different values of negative and positive charge of biomolecules as shown in figure 10(b). $I_{ON}/I_{OFF}$ sensitivities increase with the magnitude of the positive charge of biomolecules. However, for a fixed $k$ value, the proposed structure (BG-FE-HJ-STFET) reflects more change in sensitivity than previous published work. In addition, *the ION/IOFF* sensitivity of the BG-FE-HJ-STFET sensor is plotted for different dielectric constant of biomolecules for $Q_{nf} = -5 \times 10^{11}$ cm$^{-2}$, $-1 \times 10^{12}$ cm$^{-2}$, $Q_{pf} = 5 \times 10^{11}$ cm$^{-2}$, and $1 \times 10^{12}$ cm$^{-2}$ in figure 10(b). With increasing the magnitude of the dielectric constant, the sensitivity also increases. However, for particular positive charge of the biomolecules BG-FE-HJ-STFET reflects more change in sensitivity than the other works [7, 31].

The p-type channel gets depleted when negatively charged proteins are present at the $SiO_2$ interface. As a result, a decrease in channel width occurs because a higher gate voltage is required to exhaust the p-type substrate than at a neutral interface. For a metal-oxide-semiconductor structure, the voltage balance equation is represented by the notation [33].

$$V_{GS} = \psi_S + \phi_{MS} - \frac{qN_{bio}}{C_{ox}} \tag{9}$$

Where, $\psi_S$ stands for the electrostatic potential at the surface, $\phi_{MS}$ for the difference in the metal and semiconductor work functions, $N_{bio}$ for the number of charges per unit area, q for the electronic charge value, and $C_{ox}$ for the resulting capacitance per unit area, which can be expressed as follows:

Furthermore,

$$C_{ox} = \frac{k}{t_{ox}(x)} \tag{10}$$

where, $t_{ox}$(x) (dielectric thickness), $k$ (dielectric constant). In the case of a constant gate voltage and an increase in the negative charge of biomolecules, $\psi_s$ must fall in order to preserve the potential balance, as shown in equation (9). This will ultimately result in a decrease in drain current and sensitivity. Equation (9) states that given a fixed $N_{bio}$ and $V_{GS}$, an increase in $k$ results in a drop in the potential (as is illustrated in equation (11) and a rise in $\psi_{s.}$ as a result. Consequently, this increases the drain current and raises the biosensor's sensitivity. Figure 9(b) provides an illustration of this phenomenon.

$$V = -\frac{qN_{bio}}{C_{ox}} \tag{11}$$

The constant current approach can be used to calculate the threshold voltage ($V_{th}$), with the voltage at drain current $1 \times 10^{-7}$ A μm$^{-1}$ treated as $V_{th}$. The $V_{th}$ sensitivity parameter is defined as [34]:

$$\Delta V_{th} = |\Delta V_{th}(Air) - \Delta V_{th}(Bio)| \tag{12}$$

Here, the variables $\Delta V_{th}$(Air) and $\Delta V_{th}$(Bio) in this equation represent the threshold voltages when air and biomolecules, respectively, are introduced into the cavity. Furthermore, the shift in the threshold voltage that occurs when biomolecules in the air are detected is represented by $\Delta V_{th}$. The curve showing $V_{th}$ is shown in figure 11(a) inset, and it shows that when biomolecules with a higher dielectric constant are added to the cavity, $V_{th}$ drops. As a result, in comparison to air, the drain current hits $1 \times 10^{-7}$ earlier. Equation (12) is used to get the $V_{th}$ sensitivity. Among all the neutral biomolecules, the protein with $k = 8$ has the highest sensitivity. Similar to this, the inset in figure 11(b) shows a higher $V_{th}$ value for DNA with a higher charge density that is more negative and a lower $V_{th}$ value for DNA with a higher charge density that is more positive.

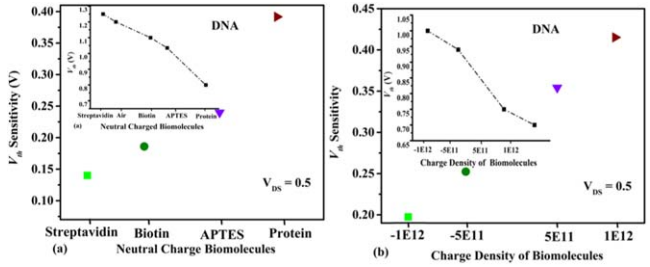


**Figure 11.** (a) The plot of sensitivity of the Threshold voltage (a) Biomolecules natural charge (b) Biomolecules with charge (DNA).

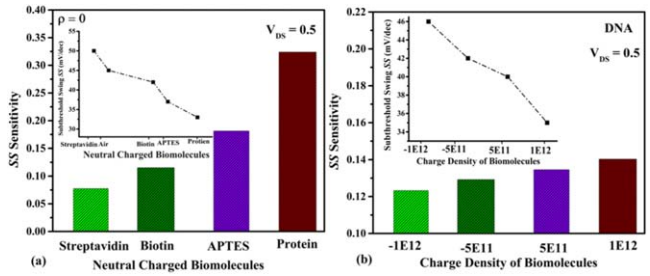


**Figure 12.** Subthreshold swing (SS) sensitivity plot of (a) neutral charge biomolecules (b) charged biomolecules (DNA) of BG-FE-HJ-STFET based biosensor at $V_{DS} = 0.5$ V and $tc = 8$ nm.

**Table 2.** Comparison of the sensitivity with the [7, 34].

| Parameters | Proposed work (Protein) | [7] | [31] | [34] |
|---|---|---|---|---|
| $I_{ON}$ Current (A/μm) | $4.25 \times 10^{-6}$ | $3.50 \times 10^{-6}$ | $4.10 \times 10^{-6}$ | $4.20 \times 10^{-6}$ |
| $I_{ON}/I_{OFF}$ Sensitivity | $4.2 \times 10^{11}$ | $2.88 \times 10^{11}$ | $1.31 \times 10^{8}$ | $2.1 \times 10^{8}$ |
| $V_{th}$ Sensitivity (V) | 0.38 V | 1.50 V | 1.65 V | 1.20 V |
| *SS* Sensitivity | 0.34 | — | — | — |

SS sensitivity is important in biosensor performance since it specifies the speed with which biomolecules are detected. *SS* sensitivity is defined as follows [34]:

$$S_{SS} = \left| \frac{(S_{SS}^{Bio} - S_{SS}^{Air})}{S_{SS}^{Air}} \right| \tag{13}$$

where $S_{SS}^{Bio}$, $S_{SS}^{Air}$ represents the cavity of the biosensor according to biomolecules, air. The *SS* sensitivity for neutral and charged biomolecules is depicted in Figures 12(a) and (b). A lower *SS* value improves the detection potential and electrical response of the BG-FE-HJ-STFET biosensor. In Figure 12(a), it is evident that increasing the dielectric constant of dielectric from air ($k = 1$) to protein ($k = 8$) reduces *SS*. It means that when the dielectric constant of the biomolecule increases, so does sensitivity. Similarly, figure 12(b) depicts the DNA of biomolecules as per the charge densities; the *SS* of the device increases as negative charge density increases and decreases as positive charge density increases. Furthermore, the suggested biosensor's SS sensitivity is improved when the charge density changes from negative to positive. A comparison of our proposed study with two additional relevant papers [7, 31] and [34] is shown in table 2.

## Modeling of surface potential

The 2D Poisson's equation (14) governs the distribution of surface potential in the gate oxide and channel region of the proposed TFET-based biosensor. Figure 13 depicts the full region (R1 to R4) considered for the analytical modeling of the surface potential [35–39].

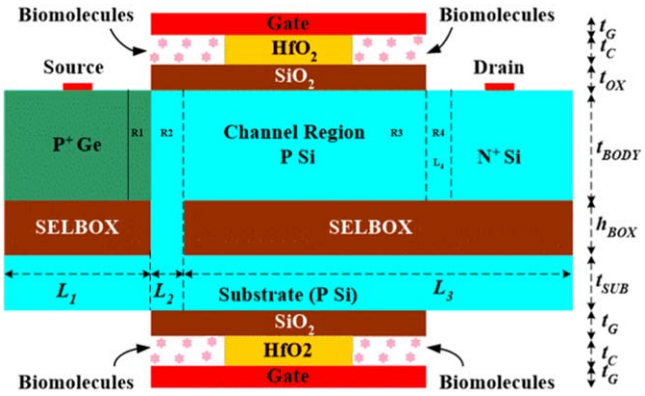


**Figure 13.** 2D structure with the full region (R1 to R4) of BG-FE-HJ-STFET.

$$\frac{\partial^2\psi_i(x,\,y)}{\partial x^2}+\frac{\partial^2\psi_i(x,\,y)}{\partial y^2}=\frac{-qN_i}{\varepsilon_{si}} \tag{14}$$

For $i=1,2,3,4$

Using the parabolic potential approximation, the 2D channel potential function $\psi_i(x,\,y)$ in the region $R_i$ (i = 1, 2, 3, 4) can be expressed as

$$\psi_i(x,\,y)=C_{0i}(x)+C_{1i}(x)y+C_{2i}(x)y^2 \tag{15}$$

where, $C_{0i}(x)$, $C_{1i}(x)$ and $C_{2i}(x)$ are arbitrary functions of $x$ to be determined by using the following boundary conditions:

$$\psi_{is}(x)=C_{0i}(x)=\psi_i(x,\,y)|_{y=0} \tag{16}$$

Where $\psi_{is}(x)$ is the surface potential:

$$\varepsilon_{Si}\frac{d\psi_i(x,\,y)}{dy}\bigg|_{y=0}=\frac{\varepsilon_{ox}}{t_{ox}}(V_{GS}-V_{fb}-\psi_{is}(x)) \tag{17}$$

$$\varepsilon_{Si}\frac{d\psi_i(x,\,y)}{dy}\bigg|_{y=t_{Si}}=\frac{\varepsilon_{ox}}{t_b}(V_{sub}-V_{ff}-\psi_i(x,\,t_{Si})) \tag{18}$$

For Region (i = 1,3,4) and (i = 2) we use (18)

$$\varepsilon_{Si}\frac{d\psi_i(x,\,y)}{dy}\bigg|_{y=t_{Si}}=0 \tag{19}$$

Where

$$V_{fb}=\phi_m-\chi_i+\frac{E_{gi}}{2}+V_{fi}$$
$$V_{fi}=V_t\ln\left(\frac{N_i}{n_i}\right) \tag{20}$$

By solving equations (14)–(20) we get

$$C_{1i}(x)=\frac{\varepsilon_{ox}}{t_{ox}\varepsilon_{Si}}(V_{GS}-V_{fb}-C_{0i}(x)) \tag{21}$$

$$C_{2i}(x)=\frac{\varepsilon_{ox}}{t_{ox}\varepsilon_{Si}}\left\{\frac{V_{G2}}{t_b}-\frac{V_{G1}}{t_{ox}}\left(1+\frac{\varepsilon_{ox}}{t_{ox}t_b}\right)+C_{0i}(x)\left[\frac{t_b-t_{ox}-\varepsilon_{ox}}{t_{ox}t_b}\right]\right\}$$
$$V_{G2}=V_{sub}-V_{ff}$$
$$V_{G1}=V_{GS}-V_{fb} \tag{22}$$

Putting (21) and (22) in (15) and applying (1) we get

$$\frac{\partial^2\psi_i(x,\,y)}{\partial x^2}\bigg|_{y=0}+\frac{\partial^2\psi_i(x,\,y)}{\partial y^2}\bigg|_{y=0}=\frac{-qN_i}{\varepsilon_{si}}\bigg|_{y=0} \tag{23}$$

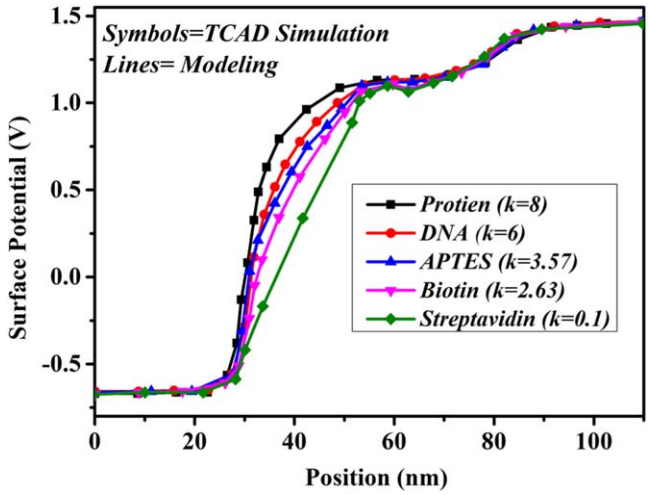


**Figure 14.** The potential plots with the device of length at $V_{DS} = 0.5$ V, $V_{GS} = 1.0$ V.

Solving (23) we get the following 1D differential equation

$$\frac{d^2\psi_{is}(x)}{dx^2} + \frac{\psi_{is}(x)}{\lambda} = \frac{qN_i}{\varepsilon_{Si}} - P_i \tag{24}$$

$$p_i = -\lambda \frac{\left(\frac{\varepsilon_{ox}}{\varepsilon_{Si} t_{Si}}\left[\frac{V_{G2}}{t_b} - \frac{V_{G1}}{t_{ox}}\left(1 + \frac{\varepsilon_{ox}}{t_{ox} t_b}\right)\right]\right)}{\left(1 + \frac{\varepsilon_{ox} t_{ox}}{2\varepsilon_{Si} t_b}\right)} \tag{25}$$

$$\lambda = \left(1 + \frac{\varepsilon_{ox} t_{Si}}{2\varepsilon_{Si} t_b}\right) \Big/ \left(\frac{t_b - t_{ox} - \varepsilon_{ox}}{t_b - t_{ox}}\right) \tag{26}$$

$$\psi_i(x, y) = K_{1i} \exp\left(\sqrt{\frac{1}{\lambda}}(x - x_{i-1})\right) - K_{2i} \exp\left(-\sqrt{\frac{1}{\lambda}}(x - x_{i-1})\right) \tag{27}$$

The value of $K_{1i}$ and $K_{2i}$ are obtained by solving the following boundary conditions

$$\psi_0 = \psi_1(0, y) = -V_T \ln(N_1/n_i) \tag{28}$$

$$\psi_1 = \psi_2(L_1, y) \tag{29}$$

$$\psi_3 = \psi_2(L_1 + L_2, y) \tag{30}$$

$$\psi_4 = \psi_3(L_1 + L_2 + L_3, y) \tag{31}$$

$$\psi_4(L_1 + L_2 + L_3 + L_4, y) = V_T \ln(N_4/n_i) + V_{DS} \tag{32}$$

$$\frac{\partial \psi_{s,i}}{\partial x}\bigg|_{x=x_i} = \frac{\partial \psi_{s,(i+1)}}{\partial x}\bigg|_{x=x_i} \quad \text{at } x = x_i \ (i = 1,\ 2,\ 3) \tag{33}$$

From boundary conditions (28)-(33) the values of constant $K_1$ and $K_2$ are obtained as

$$K_{1i} = \frac{-1}{2\sinh\left(\sqrt{\frac{1}{\lambda}}_i L_i\right)}\left(\psi_{i-1}\exp\left(-\sqrt{\frac{1}{\lambda}}_i L_i\right) - P_i\left(1 + \exp\left(-\sqrt{\frac{1}{\lambda}}_i L_i\right)\right) - \psi_i\right) \tag{34}$$

$$K_{2i} = \frac{1}{2\sinh\left(\sqrt{\frac{1}{\lambda}}_i L_i\right)}\left(\psi_{i-1}\exp\left(\sqrt{\frac{1}{\lambda}}_i L_i\right) - P_i\left(1 + \exp\left(\sqrt{\frac{1}{\lambda}}_i L_i\right)\right) - \psi_i\right) \tag{35}$$

The function of Potential with respect to region $R_i$ (i = 1, 2, 3, 4) be conveyed as,

$$\psi_i(x, y) = C_{0i}(x) + C_{1i}(x)y + C_{2i}(x)y^2 \tag{36}$$

According to the boundary condition to solve the value of $C_{oi}$, $C_{1i,}$ and $C_{2i}$, we have found the surface potential as shown in figure 14.

Figure 14 displays the fluctuation of surface potential in the device for different biomolecule dielectric constant values. The figures' symbols indicate TCAD-based simulation data, whereas the lines represent model data.

## 4. Conclusion

In this article, the dielectric modulation-based label-free bio sensing analysis of the TFET (BG-FE-HJ-STFET) structure is presented. By amplifying the low gate voltage, a ferroelectric (FE) gate stack is used to create a negative capacitance effect that increases device sensitivity. For the purpose of detecting biomolecules, TCAD simulations demonstrate subthreshold swing ($SS < 60$ mV/dec) behavior that increases the drain current, resulting in high $I_{ON}/I_{OFF}$ sensitivities of $\sim 4.2 \times 10^{11}$. The BG-FE-HJ-STFET sensor's sensitivity was primarily investigated by examining the transfer curve, current sensitivity, threshold voltage sensitivity, $I_{ON}/I_{OFF}$ sensitivity, $SS$ sensitivity with different dielectric constants, and charged biomolecules. The simulation results show that when the biomolecules' relative permittivity grows, so does their positive charge, enhancing the sensitivity of the proposed sensor. Advances in artificial biosensor technology include the transition from cell-based sensing to organ-on-chip (OoC) and paper-based biochips. Artificial biosensor technology has been used to identify, screen for drugs, detect drugs, and diagnose certain viral infections. As a result, BG-FE-HJ-STFET sensors have significant development potential and market potential. The worldwide biosensors market size was projected at USD 28.9 billion in 2023 and is predicted to reach USD 31.29 billion by the end of 2024.

## Acknowledgments

The authors would like to thank IIT (BHU) for providing the Silvaco TCAD tool.

## Data availability statement

The data cannot be made publicly available upon publication because they are not available in a format that is sufficiently accessible or reusable by other researchers. The data that support the findings of this study are available upon reasonable request from the authors.

## Funding

No funding was used in this study.

## ORCID iDs

Ashish Kumar Singh https://orcid.org/0000-0001-6143-9808
Satyabrata Jit https://orcid.org/0000-0001-6772-8117

## References

[1] Balahura L R, Stefan-Van Staden R I, Van Staden J F and Aboul-Enein H Y 2019 Advances in immunosensors for clinical applications *J. Immunoass Immunochem* **40** 40–51
[2] Vu C A and Chen W Y 2019 Field-effect transistor biosensors for biomedical applications: recent advances and future prospects *Sensors (Basel)* **19** 4214
[3] Busse S, Scheumann V, Menges B and Mittler S 2002 Sensitivity studies for specific binding reactions using the biotin/streptavidin system by evanescent optical methods *Biosens. Bioelectron.* **17** 704–10
[4] Im H, Huang X J, Gu B and Choi Y K 2007 A dielectric-modulated field-effect transistor for biosensing *Nat. Nanotechnol.* **2** 430–4
[5] Chen Y, Ren R, Pu H, Guo X, Chang J, Zhou G, Mao S, Kron M and Chen J 2017 Field-effect transistor biosensor for rapid detection of ebola antigen *Sci. Rep.* **7** 4–11
[6] Verma D, Singh K R, Yadav A K, Nayak V, Singh J, Solanki P R and Singh R P 2022 Internet of things (IoT) in nano-integrated wearable biosensor devices for healthcare applications *Biosens. Bioelectron. X* **11** 100153
[7] Mahalaxmi, Acharya B and Mishra G P 2020 Design and analysis of dual-metal-gate double-cavity charge-plasma-TFET as a label free biosensor in*IEEE Sens. J* **20** 13969–75
[8] Ajay, Narang R, Saxena M and Gupta M 2017 Modeling and simulation investigation of sensitivity of symmetric split gate junctionless FET for biosensing application in*IEEE Sens. J* **17** 4853–61
[9] Ajay, Narang R, Saxena M and Gupta M 2019 Model of GaSb-InAs p-i-n Gate all around bio tunnel FET in*IEEE Sens. J* **19** 2605–12
[10] Kim S, Ahn J H, ParK T J, Lee S Y and Choi Y K 2009 A biomolecular detection method based on charge pumping in a nanogap embedded field-effect-transistor biosensor *Appl. Phys. Lett.* **94** 1–4

[11] SarKar D and Banerjee K 2012 Proposal for tunnel-field-effect-transistor as ultra-sensitive and label-free biosensors *Appl. Phys. Lett.* **100** 14
[12] Dwivedi P and Kranti A 2018 Dielectric modulated biosensor architecture: tunneling or accumulation based transistor *IEEE Sens.* J **18** 3228–35
[13] Kannan N and Kumar M J 2013 Dielectric-modulated impact-ionization mos transistor as a label-free biosensor *IEEE Electron Device Lett.* **34** 1575–7
[14] Hraziia A *et al* 2012 An analysis on the ambipolar current in Si double-gate tunnel FETs *Solid-State Electron.* **70** 67–72
[15] Wang S, Hossain M Z, Shinozuka K, Shimizu N, Kitada S, Suzuki T, Ichige R, Kuwana A and Kobayashi H 2020 Graphene field-effect transistor biosensor for detection of biotin with ultrahigh sensitivity and specificity *Biosens. Bioelectron.* **165** 112363
[16] Vishnoi R and Kumar M J 2014 Compact analytical drain current model of gate-all-around nanowire tunneling FET *IEEE Trans. Electron Devices* **61** 2599–603
[17] Vimala P, Krishna L L and Sharma S S 2022 TFET biosensor simulation and analysis for various biomolecules *Silicon* **14** 7933–8
[18] Raad B R, Sharma D, Nigam K and Kondekar P 2016 Physics-based simulation study of highperformance gallium arsenide phosphide–indium gallium arsenide tunnel field-effect transistor *IET Micro Nano Lett.* **11** 366–8
[19] Raad B R, Nigam K, Sharma D and Kondekar P N 2016 Performance investigation of bandgap, gate material work function and gate dielectric engineered TFET with device reliability improvement *Superlattices Microstruct.* **94** 138–46
[20] Madan J, Pandey R, Sharma R and Chaujar R 2020 Investigation of electrical/analog performance and reliability of gate metal and source pocket engineered DG-TFET *Microsystem Technologies* **27** 4073–85
[21] Singh A K, Tripathy M R, Baral K, Singh P K and Jit S 2020 Investigation of DC, RF and linearity performances of a back-gated (BG) heterojunction (HJ) TFET-on-selbox-substrate (STFET): introduction to a BG-HJ-STEFT based CMOS inverter *Microelectronics* J **102** 104775
[22] ATLAS Device Simulator Software *SILVACO Int., Santa Clara, CA, USA, 2018*
[23] Biswas A, Dan S S, Royer C L, Grabinski W and Ionescu A M 2012 TCAD simulation of SOI TFETs and calibration of non-local band-to-band tunneling model *Microelectron. Eng.* **98** 334–7
[24] Singh A K, Kumar R, Maity H, Singh P and Singh S 2024 Analog and linearity performance analysis of ferroelectric vertical tunnel field effect transistor with and without source pocket *Int. J. Numer. Modell. Electron. Networks Devices Fields* **37** 4
[25] Zhang Q, Zhao W and Seabaugh A 2006 Low-subthreshold-swing tunnel transistors *IEEE Electron Device Lett.* **27** 297–300
[26] Singh A K, Tripathy M R, Baral K, Singh P K and Jit S 2020 Impact of interface trap charges on device level performances of a lateral/vertical gate stacked Ge / Si TFET - on - SELBOX - substrate *Appl. Phys.* A **126** 1–11
[27] Tripathy M R *et al* 2020 Device and circuit-level assessment of GaSb/Si heterojunction vertical tunnel-FET for low-power applications in*IEEE Trans. Electron Devices* **67** 1285–92
[28] Singh A K, Tripathy M R, Baral K and Jit S 2022 GaSb/GaAs Type-II heterojunction TFET on SELBOX substrate for dielectric modulated label-free biosensing application in*IEEE Trans. Electron Devices* **69** 5185–92
[29] Singh S, KondeKar P N and Jaiswal N K 2016 Label-free biosensor using nanogap embedded dielectric modulated SchottKy tunneling source impact ionization MOS *Microelectron. Eng.* **149** 129–34
[30] Verma M, TirKey S, Yadav S, Sharma D and Yadav D S 2017 Performance assessment of a novel vertical dielectrically modulated TFET based biosensor *IEEE Trans. Electron Devices* **64** 3841–8
[31] Goswami R and Bhowmick B 2019 Comparative analyses of circular gate TFET and heterojunction TFET for dielectric-modulated label-free biosensing *in IEEE Sensors Journal* **19** 9600–9
[32] Narang R, Saxena M and Gupta M 2015 Comparative analysis of dielectric-modulated FET and TFET-based biosensor *IEEE Trans. Nanotechnol.* **14** 427–35
[33] Tsividis Y 1990 *Operation and Modelling of the MOS Transistor* 2nd ed (Oxford University Press)
[34] Chong C, Liu H, Wang S and Chen S 2021 Simulation and performance analysis of dielectric modulated dual source trench gate TFET *Biosensor,// Nanoscale Res. Lett.* **16** 1
[35] Upasana, Narang R, Saxena M and Gupta M 2015 Modeling and TCAD assessment for gate material and gate dielectric engineered TFET architectures: circuit-level investigation for digital applications in*IEEE Trans. Electron Devices* **62** 3348–56
[36] Wadhwa G and Raj B 2022 Surface potential modeling and simulation analysis of dopingless TFET biosensor *Silicon* **14** 2147–56
[37] Madan J, Gupta R S and Chaujar R 2016 Mathematical modeling insight of hetero gate dielectric-dual material gate-GAA-tunnel FET for VLSI/analog applications *Microsystem Technologies* **23** 4091–4098
[38] Dewan B, Chaudhary S, Singh D and Yadav M 2023 A physics-based model of dielectric modulated TFET biosensor considering non-ideal hybridization issue *Micro and Nanostructures* **183** 207668
[39] Talukdar J, Rawat G and Mummaneni K 2023 Highly sensitivity non-uniform tunnel FET based biosensor using source engineering *Materials Science and Engineering* B **293** 116455